Applied Physics Letters

RESEARCH ARTICLE | MAY 22 2023

Improving crystal quality of β-phase MgGaO thin films by using low-temperature homo-buffer layer

Chengyun Shou; Tianchen Yang; Abdullah Almujtabi; ... et. al

Appl. Phys. Lett. 122, 212101 (2023)
https://doi.org/10.1063/5.0147948

CrossMark

Downloaded from http://pubs.aip.org/aip/apl/article-pdf/doi/10.1063/5.0147948/17720396/212101_1_5.0147948.pdf

Time to get excited.
Lock-in Amplifiers – from DC to 8.5 GHz
Find out more
Zurich Instruments

AIP Publishing

Applied Physics Letters ARTICLE pubs.aip.org/aip/apl

Improving crystal quality of β-phase MgGaO thin films by using low-temperature homo-buffer layer

Cite as: Appl. Phys. Lett. **122**, 212101 (2023); doi: 10.1063/5.0147948
Submitted: 27 February 2023 · Accepted: 1 May 2023 ·
Published Online: 22 May 2023

View Online

Export Citation

CrossMark

Chengyun Shou,[1] Tianchen Yang,[1] Abdullah Almujtabi,[1] Theodore Yang,[1,2] Yuan Li,[1] Quazi Sanjid Mahmud,[1] Mingjie Xu,[3] Jian-Guo Zheng,[3] and Jianlin Liu[1,a)]

AFFILIATIONS

[1]Department of Electrical and Computer Engineering, University of California, Riverside, California 92521, USA
[2]Martin Luther King High School, Riverside, California 92508, USA
[3]Irvine Materials Research Institute (IMRI), University of California, Irvine, California 92697, USA

[a)]Author to whom correspondence should be addressed: jianlin@ece.ucr.edu. **Tel.:** 1-9518277131. **Fax:** 1-9518272425

ABSTRACT

Ultra-wide bandgap (UWBG) semiconductors are promising for many applications, such as power electronics and deep-ultraviolet photonics. In this research, UWBG β-phase magnesium gallium oxide (MgGaO) thin films with a bandgap of 5.1 eV were grown using low-temperature homo-buffer layers in a plasma-assisted molecular beam epitaxy system. The role of the growth temperature and thickness of low-temperature buffer layer on the quality of the active layer was studied using x-ray diffraction and transmission electron microscopy and by analyzing the properties of metal–semiconductor–metal photodetector devices based on these films. It is found that lower buffer growth temperature at 300 °C leads to higher crystal quality of active layer. For the same low buffer growth temperature, different crystal quality in the active layer is attained with different buffer layer thickness. A buffer layer thickness at 40 nm has the best active layer quality with the highest photo current under 265 nm illumination and long decay time as a result of reduced recombination of photo-generated carriers through fewer defects in the active layer.

Published under an exclusive license by AIP Publishing. https://doi.org/10.1063/5.0147948

Ultra-wide bandgap (UWBG) semiconductors with a bandgap larger than 4 eV[1–4] have attracted much attention for promising applications in power electronics[5,6] and deep ultraviolet (UV) photonics.[7] Among these UWBG semiconductors, β-phase gallium oxide (Ga_2O_3) with an optical bandgap of ∼4.9 eV was studied extensively in recent years due to its direct bandgap, high critical electric field strength, and high figure of merits for next-generation deep-UV and power devices.[8–10] To further enhance the performance of electronic and optoelectronic devices, suitable wider bandgap material that is compatible with and can form high-quality heterostructures with Ga_2O_3 is in demand. Recently, we proposed to use ternary alloy magnesium gallium oxide $(Mg_xGa_{1-x})_2O_3$ as a viable candidate.[11] By tuning the Mg composition in the alloy, the bandgap is expected to be tuned with a wide range between ∼4.9 and 7.8 eV. In this prior study,[11] β-phase $(Mg_xGa_{1-x})_2O_3$ alloys were grown on c-plane sapphire substrates, which are commonly used to grow various UWBG semiconductors including β-Ga_2O_3. Although direct band property with a bandgap up to 5.2 eV was demonstrated, the $(Mg_xGa_{1-x})_2O_3$ films were directly grown on the substrates without any buffer layers; in turn, the crystal quality is less satisfied due to the large lattice mismatch between the film and substrate.[12,13]

In this study, we aimed at significantly improving the crystal quality of β-phase $(Mg_{0.074}Ga_{0.926})_2O_3$ thin films by using low-temperature homo-buffer layer technique. Low-temperature buffer layer, which consists of high-density point defects, is effective in the reduction of dislocations in the active layer grown on top. This technique had been successfully adopted in other semiconductor systems to improve their crystal quality, including GaN[13–15] and ZnO.[16–20] Here, plasma-assisted molecular beam epitaxy (MBE) is used to deposit low-temperature MgGaO buffer layer between c-plane sapphire substrate and β-$(Mg_{0.074}Ga_{0.926})_2O_3$ active layer. The role of different growth temperature and thickness of the buffer layers on the improvement of the quality of the active layers is studied in detail.

C-plane sapphire substrate was cleaned using piranha solution (H_2SO_4: H_2O_2 = 5:3) under 200 °C for 20 min to remove any organic residue on the surface and then rinsed by DI water and placed inside an ultrasonic cleaner for 5 min. After blown-dry using a nitrogen gun, the substrate was placed onto the substrate holder and then loaded into the load lock of MBE chamber (SVT Associates, Inc.). 6N Ga and 4N Mg from Alfa Aesar were used for sample growth. Effusion cell temperatures were set to 750 °C for Ga and 400 °C for Mg for both buffer layer and active layer growth. The oxygen flow rate was set to

Published under an exclusive license by AIP Publishing

Downloaded from http://pubs.aip.org/aip/apl/article-pdf/doi/10.1063/5.0147948/17720396/212101_1_5.0147948.pdf

2.5 sccm, and RF power was set to 400 W. For the pre-growth annealing process, the substrate temperature was set to 800 °C for 15 min and then lowered for the low-temperature buffer layer growth at 300–500 °C. All active MgGaO layers were grown at 650 °C for two hours, followed by 20 min post-growth annealing at 700 °C under oxygen environment. A test buffer-layer sample was grown for one hour to determine the growth rate of the low-temperature buffer layer. Samples of different growth time for different buffer layer thickness were grown depending on the growth rate from the test sample. Under the same buffer growth temperature of 300 °C, 0, 1, 5, 10, 20, 30, and 40 nm buffer layer thicknesses were selected for comparison, while under the same buffer layer thickness of 40 nm, different low buffer growth temperature range between 300 and 500 °C was studied. The active layers among all the samples have approximately the same thickness of ∼160 nm. Thickness data were also confirmed from post-growth measurement using a Nikon Profilm3D profilometer.

The composition of MgGaO thin films was analyzed using a Bruker energy dispersive x-ray (EDX) spectroscopy analytical system. Figure 1(a) shows the EDX result of the $(Mg_{0.074}Ga_{0.926})_2O_3$ sample with a buffer layer of 40 nm, and the inset graph is the scanning electron microscope (SEM) image of the sample, which was acquired using a TESCAN Vega 3 SBH SEM system, showing that the film is relatively flat and continuous. EDX peaks at 1.1 and 9.2 keV are corresponding to Ga $L\alpha$, and $K\alpha$, respectively, and peaks at 0.5 and 1.2 keV are corresponding to oxygen $K\alpha$ and Mg $K\alpha$, respectively. Aluminum $K\alpha$ peak was also collected at 1.5 keV, which originates from the c-sapphire. Figure S1 in the supplementary material shows similar EDX and SEM results for other samples with different buffer layer thicknesses. The average atomic percentage for Ga and Mg is determined by EDX to be 85 and 15 at. %, respectively, for all samples. The atomic composition was also analyzed using x-ray photoelectron spectroscopy (XPS), as shown in Fig. S2 in the supplementary material. Ga, Mg, and O atomic percentage from XPS is estimated to be 31.0, 2.5, and 66.5 at. %, respectively. This suggests that our MgGaO alloy is oxygen-rich. XPS composition data may be more acceptable than EDX data here because XPS collects signals from the surface and large area of the sample, while EDX signal is restricted in small area and much depth of the sample. Figure 1(b) shows low magnification cross-sectional transmission electron microscopy (TEM) image of the $(Mg_{0.074}Ga_{0.926})_2O_3$ sample with 40 nm buffer layer. The TEM sample was coated with (bright) carbon and (dark) metal layers to prevent charging effect and protect the TEM lamella. The selected area electron diffraction (SAED) pattern was

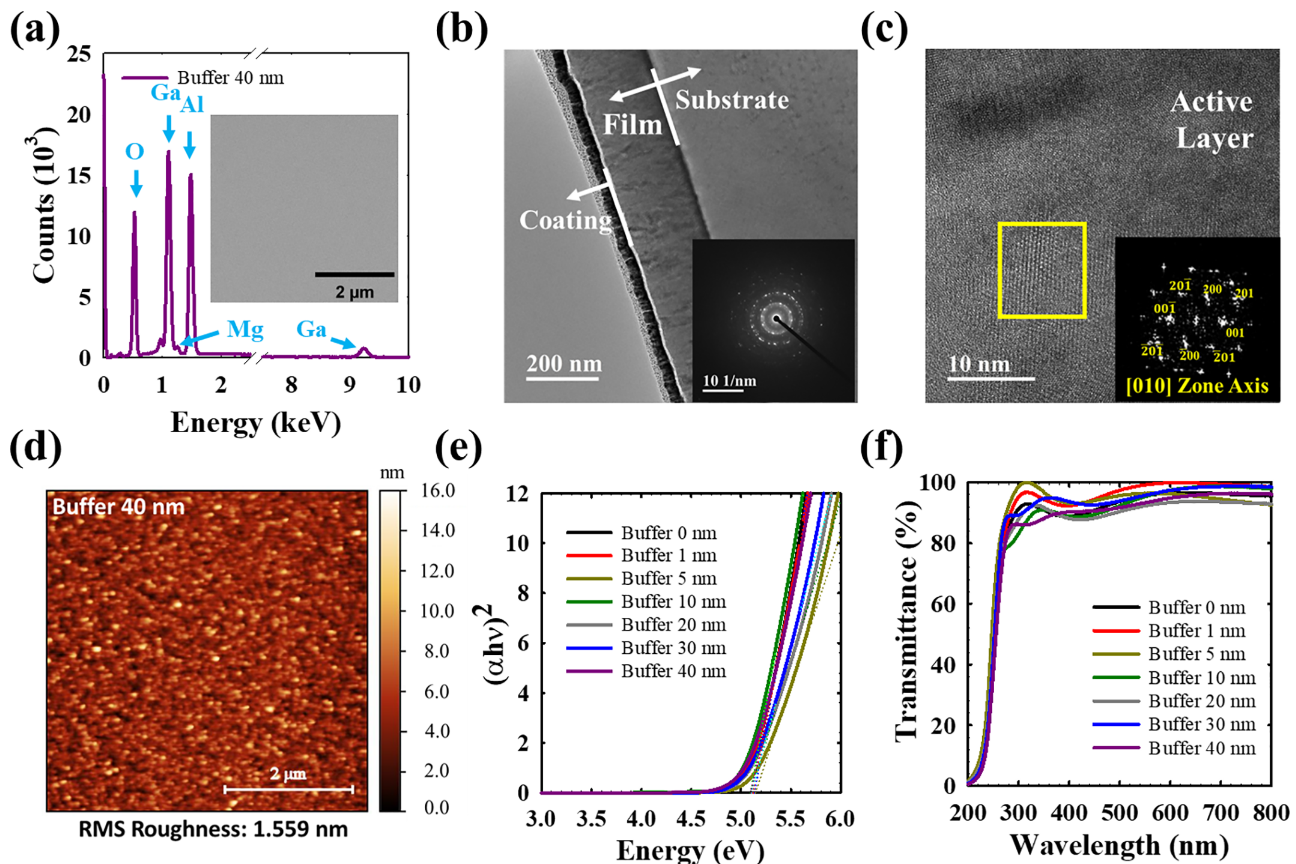

FIG. 1. (a) EDX spectrum and SEM image of an $(Mg_{0.074}Ga_{0.926})_2O_3$ sample with 40 nm buffer. (b) Low magnification cross-sectional TEM image of $(Mg_{0.074}Ga_{0.926})_2O_3$ sample with 40 nm buffer layer and corresponding SAED pattern from film area. (c) HRTEM image of the active layer of $(Mg_{0.074}Ga_{0.926})_2O_3$ sample and corresponding fast Fourier transform (FFT) pattern of the area marked with square solid lines. (d) AFM image of an $(Mg_{0.074}Ga_{0.926})_2O_3$ sample containing 40 nm buffer. (e) Tauc plot absorption spectra and (f) transmittance spectra for all samples.

Downloaded from http://pubs.aip.org/aip/apl/article-pdf/doi/10.1063/5.0147948/17720396/212101_1_5.0147948.pdf

Published under an exclusive license by AIP Publishing

acquired from the film using an electron beam of approximately 100 nm in diameter and is shown in the inset of Fig. 1(b). The diffraction spots form several diffraction rings in the pattern, indicating that the thin film including both active layer and buffer layer contains polycrystalline grains, and the crystal structure of these grain is similar to the β-phase Ga_2O_3. Figure 1(c) shows high-resolution TEM (HRTEM) image of the active layer, showing lattice fringes clearly, which represent atomic planes well aligned with the electron beam. The inset shows the fast Fourier transform (FFT) pattern of the selected area with two-dimensional fringes. The FFT pattern indicates the [010] zone axis of β-phase $(Mg_{0.074}Ga_{0.926})_2O_3$. The TEM results suggest that the active layer has better quality than the buffer layer. Figure 1(d) shows an AFM image of the sample with 40 nm buffer layer using a Dimension 5000 AFM system, and the root mean square (RMS) roughness is estimated to be 1.559 nm. AFM characterization of other samples show similar morphology and RMS roughness results, as shown in Fig. S3 in the supplementary material.

Absorption spectroscopy was used to obtain the optical bandgap of each sample. First, the absorbance data were measured using an Agilent Cary 5000 double beam UV/VIS/NIR spectrometer from 200 to 800 nm, and then photon energy for each incident wavelength is calculated from the equation $E = h\nu = \frac{1240}{\lambda\,[\mathrm{nm}]}$ [eV], where h is the Planck's constant, ν is the frequency, and λ is the incident wavelength. The absorbance data were converted into absorption coefficient using the equation $\alpha = 2.303 \times \frac{A}{t}$, where α is the absorption coefficient, A is the absorbance, and t is the film thickness. Figure 1(e) shows Tauc plot absorption spectra of all samples. Each curve was fitted using linear regression with $r^2 = 0.999$ from the Tauc plot to extract the optical bandgap, yielding a value of 5.1 eV for all samples. Transmittance data were calculated from absorbance using the equation[21] $A = 2 - \log(\%T)$, where T is the transmittance. As seen in Fig. 1(f), all samples have high transmittance of ~90% at a spectral range above 300 nm with no Urbach tail.[22]

Figure 2(a) shows XRD pattern in $\theta/2\theta$ scan mode of all MgGaO samples using a PANalytical Empyrean Series 2 XRD system with Cu K α x-ray ($\lambda = 0.15405$ nm), which confirms the $(\bar{2}01)$ orientation β-$(Mg_{0.074}Ga_{0.926})_2O_3$ for all samples. Two theta peaks at ~19.0°, ~38.3°, and ~58.9° are corresponding to $(\bar{2}01)$, $(\bar{4}02)$, and $(\bar{6}03)$ orientations of β-$(Mg_{0.074}Ga_{0.926})_2O_3$. The 2θ peak at ~42° is from c-plane sapphire substrate, and 2θ peak at ~44.7° is from aluminum XRD holder. XRD rocking curve measurement on $(\bar{4}02)$ orientation was also performed on the $(Mg_{0.074}Ga_{0.926})_2O_3$ samples with different buffer layer thicknesses using a Rigaku SmartLab X-ray diffractometer. Figure 2(b) shows XRD rocking curves of the samples, which were then fitted using the Gaussian method to extract full width at half maximum (FWHM). The FWHM of samples with a buffer of 0, 1, 5, 10, 20, 30, and 40 nm are 0.073 23°, 0.075 06°, 0.078 97°, 0.080 00°, 0.086 74°, 0.8810°, and 0.083 82°, respectively. The inset in Fig. 2(b) shows the XRD rocking curve FWHM as a function of buffer thickness. The FWHM values are usually dependent on the crystal's quality, and the better the film quality, the smaller the FWHM. Here, the FWHM values represent an overall quality from weighted contributions from both lower-quality buffer layer and higher-quality active layer. The FWHM value for the reference sample without any buffer layer sets up a baseline quality of the active layer. For samples with buffer layer thickness from 0 to 30 nm, the FWHM broadens as the buffer layer thickness increases. This may be due to the dominant contribution of the lower-quality buffer layer, while the quality of the active layer may not have been enhanced significantly with the buffer layers less than 30 nm, resulting in an overall larger FWHM values compared to 0 nm buffer layer sample. As the low-temperature MgGaO buffer layer thickness increases within ~30 nm, the signal from the lower-quality buffer layer increases, leading to the increase in the FWHM of the XRD rocking curves. As the low-temperature buffer layer thickness increases beyond 30 nm, the quality of the active layer has evidently improved, which results in the decrease in the FWHM of the XRD rocking curve. This XRD result is in good agreement with

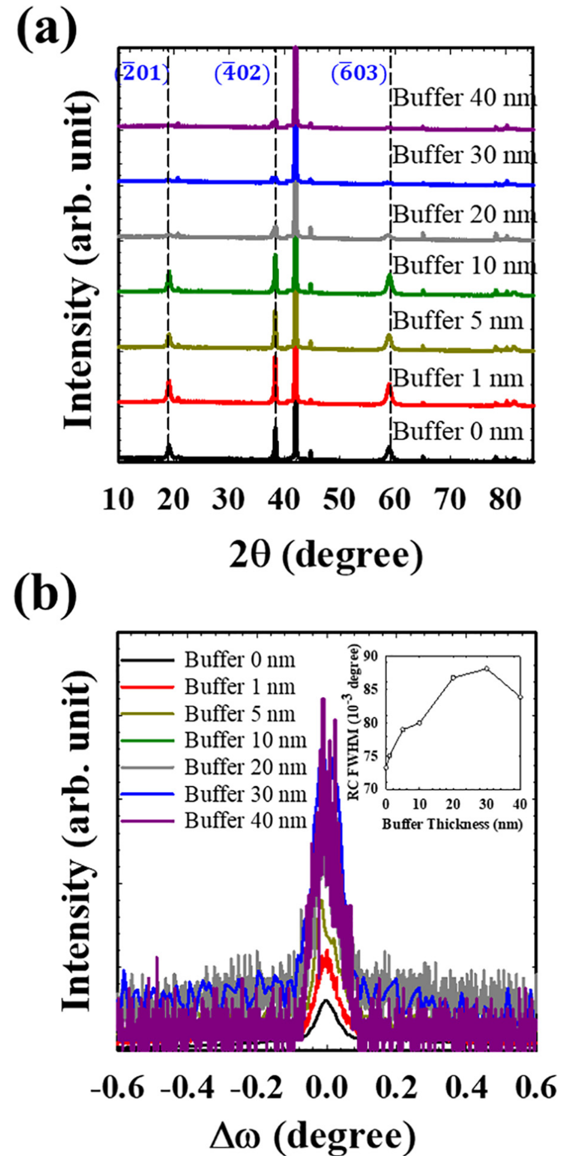

FIG. 2. (a) XRD pattern in $\theta/2\theta$ scan mode showing that all MgGaO samples are β-phase with $(\bar{2}01)$ orientation. (b) XRD rocking curves of $(Mg_{0.074}Ga_{0.926})_2O_3$ samples $(\bar{4}02)$ peak and FWHM fitted with Gaussian method are plotted in the inset graph.

Published under an exclusive license by AIP Publishing

Downloaded from http://pubs.aip.org/aip/apl/article-pdf/doi/10.1063/5.0147948/17720396/212101_1_5.0147948.pdf

current–voltage characteristics and decay time performances of the photodetectors presented next.

The enhanced quality of the $(Mg_{0.074}Ga_{0.926})_2O_3$ active layer as a result of low-temperature buffer was also studied using metal–semiconductor–metal (MSM) photodetectors. In a clean room, samples were cleaned using isopropyl alcohol (IPA) and acetone, and then a layer of AZ 5214 photoresist was coated on top of the film, followed by a soft bake at 110 °C for 1 min. The MSM photodetector mask has 15 digits on each side with finger size of 220 μm length, 5 μm width, and 3 μm spacing. The mask was placed inside a Karl Suss Mask Aligner to expose the pattern to the sample. Samples after exposure were placed into the AZ400 solution for 1 min to perform the development process. After development, plasma etching was performed inside an AJA sputtering system to remove any contamination on the film surface, and then a platinum layer with a thickness of 20 nm was deposited onto the sample, followed by the deposition of a gold layer of 100 nm on top using an electron-beam evaporator. After the deposition process, samples were placed inside acetone to perform the liftoff process to complete the device fabrication.

Figure 3(a) shows a schematic of the MSM photodetector with an interdigitated metal contact structure. Figure 3(b) shows photocurrent spectra of the MSM device of the sample with 40 nm buffer under different applied voltages. Two peaks are shown at ~258 nm (4.81 eV) and ~490 nm (2.53 eV). The peak at 258 nm may have originated from near-band edge absorption process, while the peak at 490 nm may be related to the transitions between the oxygen vacancies as donor states and gallium vacancies as acceptor states.[11,23–25] Figure S4 in the supplementary material shows photocurrent spectra of samples with other buffer layer thicknesses, showing similar results. The measurement of current–voltage (I–V) characteristics was performed on a Signatone S1045 probe station with a hot chuck and an Agilent 4155C semiconductor parameter analyzer. A 265 nm wavelength light source was also installed on the probe station to measure the photocurrent of the devices. Dark currents for all samples were below 20 nA, which are below the limitation of our instrument. Figure 3(c) shows I–V characteristics of MSM devices based on $(Mg_{0.074}Ga_{0.926})_2O_3$ thin films with different buffer layer thicknesses under 265 nm illumination from −20 to 20 V. I–V plots show back-to-back Schottky diode characteristics, and the current increases with the increase in the buffer layer thickness under the same voltage. Figure 3(d) shows the current box plot at 20 V under 265 nm illumination for devices with different buffer layer thicknesses by measuring

Downloaded from http://pubs.aip.org/aip/apl/article-pdf/doi/10.1063/5.0147948/17720396/212101_1_5.0147948.pdf

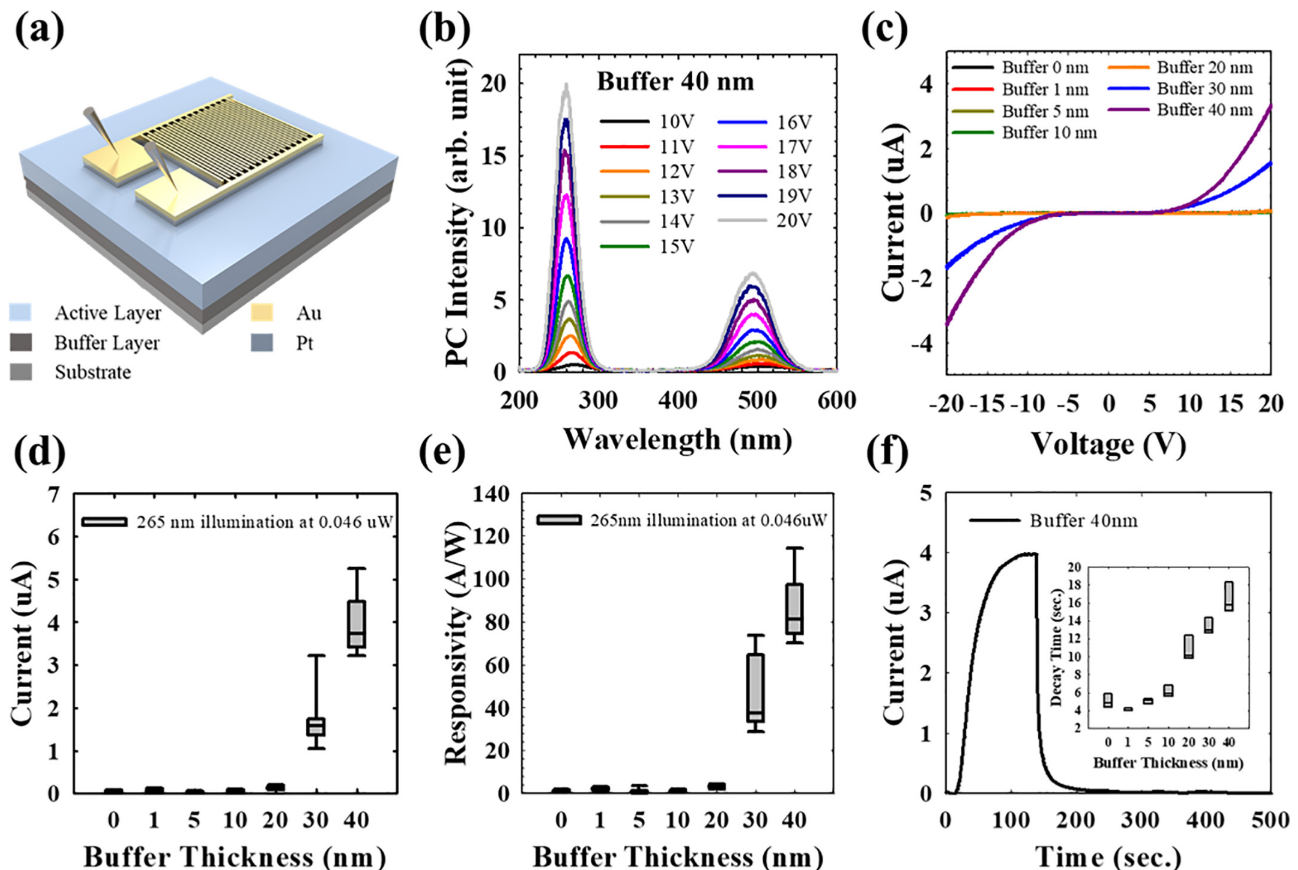

FIG. 3. (a) Schematic of interdigitated MSM photodetector. (b) Photocurrent spectra of the device sample with 40 nm buffer under different bias. Two peaks at 258 and 490 nm are observed. (c) Current–voltage plot, (d) photocurrent box plot, and (e) responsivity under 265 nm illumination for samples with different buffer thicknesses. (f) Decay time curve under 265 nm illumination for the sample with 40 nm buffer, and the inset shows decay time box plot for all samples.

Published under an exclusive license by AIP Publishing

over 20 data points for each device. The average photocurrent increases as the increase in buffer layer thickness. Specifically, the average current is below 130 nA in devices with buffer layer thickness less than 20 nm, and for buffer layer thickness at 30 and 40 nm, the current increases to 1.6 and 3.7 μA, respectively. When the buffer layer thickness increases above 30 nm, the film quality improves because of fewer defects or traps, which means less recombination inside the active layer and more electrons and holes collected by the two electrodes. The responsivity, R_λ, is then calculated by using[26] $R_\lambda = \frac{\Delta I}{P}$, where ΔI is the photocurrent, and P is the incident light power illuminating the active layer. The total light power penetrating the active layer is estimated to be 0.046 μW. Figure 3(e) shows the box plot of responsivity in devices with different buffer layer thicknesses. The average responsivity for 30 nm buffer and 40 nm buffer is 37 and 81 A/W, respectively.

Figure 3(f) shows the time response of photocurrent in a device with buffer layer thickness of 40 nm, and the inset shows the box plot of decay time for all samples. A 265 nm light source, controlled by pulse generator, was turned on for 130 s and then turned off. Voltage of 20 V was applied to the MSM photodetector, and the photocurrent was collected by an Agilent 4155C semiconductor parameter analyzer. The decay time is defined as the time needed for the current to decay to its value of $1/e$. It was fitted using the exponential equation $I = I_0 e^{-t/\tau}$, where I is the current, I_0 is the photocurrent at the steady state, τ is the lifetime of the carriers, and t is the time. When the light source is removed, the duration of decay time is related to the number of photo carriers that can transport from the semiconductor to electrodes, which is affected by carrier trapping due to the presence of defects. As seen in the inset of Fig. 3(f), as the buffer layer thickness increases, the decay time increases. Higher-quality $(Mg_{0.074}Ga_{0.926})_2O_3$ active layer has less defects in it, leading to less trapping of photocarriers, in turn, slower reduction of photocurrent and longer decay time.

In addition to the studies of $(Mg_{0.074}Ga_{0.926})_2O_3$ film quality change as a function of low-temperature homo-buffer thickness, the role of different growth temperature for the same buffer layer thickness on the quality of the active layer was also investigated. Figure 4(a) shows the photocurrent decay time in the MSM devices with the same buffer layer thickness at 40 nm but at different growth temperatures. As the buffer growth temperature increases from 300 to 400 °C, and to 500 °C, the decay time decreases from 15.8 to 11.2, and to 8.8 s, respectively. This suggests that the $(Mg_{0.074}Ga_{0.926})_2O_3$ active layer on a buffer grown at lower temperature has higher quality. Lower buffer growth temperature results in higher defect density in the buffer, which is more effective in enhancing the quality of the active layer on

Downloaded from http://pubs.aip.org/aip/apl/article-pdf/doi/10.1063/5.0147948/17720396/212101_1_5.0147948.pdf

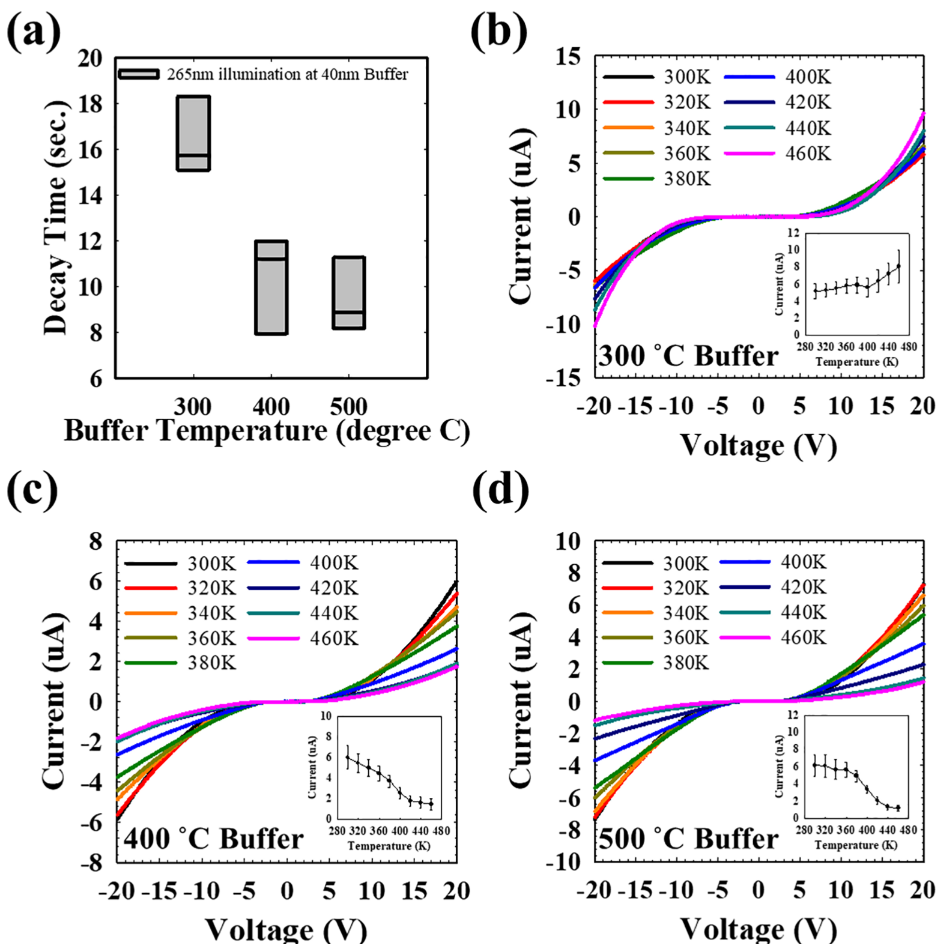

FIG. 4. (a) Decay time for MSM devices based on MgGaO films with the same buffer thickness of 40 nm and different buffer layer growth temperature. Temperature-dependent I–V characteristics under 265 nm illumination for samples with 40 nm buffer grown at (b) 300, (c) 400, and (d) 500 °C. Insets in (b), (c), and (d) show photocurrent at 20 V under 265 nm illumination as a function of measurement temperature.

Published under an exclusive license by AIP Publishing

top. Figure 4(b) shows the temperature dependent I–V characteristics of a MSM device with 300 °C buffer, and the inset summarizes the current at 20 V, which increases with the increase in the measurement temperature. On the other hand, current decreases with the increase in the measurement temperature for devices with buffer layers grown at 400 and 500 °C, as seen in Figs. 4(c) and 4(d), respectively. This could be due to the competing current transport mechanisms between thermionic emission and trap-assisted recombination[27] inside the active layer. MSM photodetector current transport mechanism is usually dominated by thermionic emission on both sides of the metal–semiconductor contact.[28–31] Charge carriers gain more energy when the temperature increases, and more carriers can jump through the barrier height, resulting in a larger current density. On the other hand, as the temperature increases, more phonon-assisted carrier traps activate, which results in the reduction of the current. In this case, the dominant mechanism is phonon-assisted carrier traps for the device samples with the buffer layer temperatures at 400 and 500 °C, while the device with the buffer layer temperature at 300 °C is dominated by thermionic emission due to the reduction of traps inside the active layer.

In summary, low-temperature homo-buffer layer was used to improve the crystal quality of β-phase $(Mg_{0.074}Ga_{0.926})_2O_3$ active layer. XPS results show an average atomic percentage composition of 31.0 at. % for Ga, 2.5 at. % for Mg, and 66.5 at. % for O. All samples exhibit β-phase. For $(Mg_{0.074}Ga_{0.926})_2O_3$ samples grown with buffer layer at 300 °C, XRD rocking curves show that the quality of the $(Mg_{0.074}Ga_{0.926})_2O_3$ active layer depends on the thickness of the low-temperature buffer, and it reaches the best quality when the thickness is 40 nm. It is also in agreement with the fact that the MSM device fabricated based on the film grown on the 40 nm buffer has the highest photocurrent and longest decay time among all samples. It was also shown that with the same buffer thickness of 40 nm, $(Mg_{0.074}Ga_{0.926})_2O_3$ film grown with lower buffer growth temperature at 300 °C exhibits higher crystalline quality than those on the buffer with higher growth temperature. This study provides an effective way to improve the quality of UWBG MgGaO thin films for deep-UV photonic applications.

See the supplementary material for EDX spectra, SEM images, XPS spectra, AFM images, and photocurrent spectra of samples with other buffer thicknesses.

This work was supported by the National Science Foundation (No. ECCS-2105566). The authors acknowledge the use of the XPS instrument at UC Riverside, which is supported by the National Science Foundation (No. DMR-0958796), and the use of facilities and instrumentation at the UC Irvine Materials Research Institute (IMRI), which is supported in part by the National Science Foundation through the UC Irvine Materials Research Science and Engineering Center (No. DMR-2011967).

AUTHOR DECLARATIONS

Conflict of Interest

The authors have no conflicts to disclose.

Author Contributions

Chengyun Shou: Conceptualization (lead); Data curation (lead); Formal analysis (lead); Investigation (lead); Methodology (lead); Project administration (lead); Resources (lead); Software (lead); Supervision (lead); Validation (lead); Visualization (lead); Writing – original draft (lead); Writing – review & editing (equal). **Tianchen Yang:** Conceptualization (supporting); Data curation (supporting); Investigation (supporting); Software (supporting); Supervision (supporting); Writing – review & editing (supporting). **Abdullah Almujtabi:** Data curation (supporting); Software (supporting). **Theodore Yang:** Data curation (supporting); Software (supporting). **Yuan Li:** Software (supporting). **Quazi Sanjid Mahmud:** Software (supporting). **Mingjie Xu:** Formal analysis (supporting); Software (supporting); Writing – review & editing (supporting). **Jian-Guo Zheng:** Formal analysis (supporting); Software (supporting); Writing – review & editing (supporting). **Jianlin Liu:** Conceptualization (lead); Funding acquisition (lead); Investigation (supporting); Project administration (lead); Supervision (lead); Writing – review & editing (equal).

DATA AVAILABILITY

The data that support the findings of this study are available within the article and its supplementary material.

REFERENCES

[1] D. Brunner, H. Angerer, E. Bustarret, F. Freudenberg, R. Höpler, R. Dimitrov, O. Ambacher, and M. Stutzmann, J. Appl. Phys. **82**(10), 5090 (1997).
[2] J. Muth, J. D. Brown, M. Johnson, Z. Yu, R. Kolbas, J. Cook, and J. Schetzina, MRS Internet J. Nitride Semicond. Res. **4**(S1), 502 (1999).
[3] T. S. T. Suzuki, H. Y. H. Yaguchi, H. O. H. Okumura, Y. I. Y. Ishida, and S. Y. S. Yoshida, Jpn. J. Appl. Phys., Part 2 **39**(6A), L497 (2000).
[4] S. A. Nikishin, M. Holtz, and H. Temkin, Jpn. J. Appl. Phys., Part 1 **44**(10R), 7221 (2005).
[5] A. Hickman, R. Chaudhuri, S. J. Bader, K. Nomoto, K. Lee, H. G. Xing, and D. Jena, IEEE Electron Device Lett. **40**(8), 1293 (2019).
[6] Y. Ohmaki, M. Tanimoto, S. Akamatsu, and T. Mukai, Jpn. J. Appl. Phys., Part 2 **45**(11L), L1168 (2006).
[7] Y. Zhang, S. Krishnamoorthy, F. Akyol, A. A. Allerman, M. W. Moseley, A. M. Armstrong, and S. Rajan, Appl. Phys. Lett. **109**(12), 121102 (2016).
[8] K. D. Chabak, N. Moser, A. J. Green, D. E. Walker, Jr., S. E. Tetlak, E. Heller, A. Crespo, R. Fitch, J. P. McCandless, and K. Leedy, Appl. Phys. Lett. **109**(21), 213501 (2016).
[9] J. Yang, S. Ahn, F. Ren, S. Pearton, S. Jang, and A. Kuramata, IEEE Electron Device Lett. **38**(7), 906 (2017).
[10] Y. Lv, X. Zhou, S. Long, Y. Wang, X. Song, X. Zhou, G. Xu, S. Liang, Z. Feng, and S. Cai, Phys. Status Solidi RRL **14**(3), 1900586 (2020).
[11] T. Yang, C. Shou, L. Xu, J. Tran, Y. He, Y. Li, P. Wei, and J. Liu, "Metal–semiconductor–metal photodetectors based on β-MgGaO thin films," ACS Appl. Electron. Mater. **5**(4), 2122–2130 (2003).
[12] Y. Chen, H. Liang, X. Xia, P. Tao, R. Shen, Y. Liu, Y. Feng, Y. Zheng, X. Li, and G. Du, J. Mater. Sci.: Mater. Electron. **26**(5), 3231 (2015).
[13] S. Nakagomi and Y. Kokubun, J. Cryst. Growth **349**(1), 12 (2012).
[14] S. Hersee, J. Ramer, K. Zheng, C. Kranenberg, K. Malloy, M. Banas, and M. Goorsky, J. Electron. Mater. **24**(11), 1519 (1995).
[15] T. Wang, T. Shirahama, H. Sun, H. Wang, J. Bai, S. Sakai, and H. Misawa, Appl. Phys. Lett. **76**(16), 2220 (2000).
[16] J. Yan, Y. Lu, Y. Liu, H. Liang, B. Li, D. Shen, J. Zhang, and X. Fan, J. Cryst. Growth **266**(4), 505 (2004).
[17] F. Xiu, Z. Yang, D. Zhao, J. Liu, K. A. Alim, A. A. Balandin, M. E. Itkis, and R. C. Haddon, J. Cryst. Growth **286**(1), 61 (2006).
[18] T. Nakamura, Y. Yamada, T. Kusumori, H. Minoura, and H. Muto, Thin Solid Films **411**(1), 60 (2002).
[19] V. Khranovskyy, R. Minikayev, S. Trushkin, G. Lashkarev, V. Lazorenko, U. Grossner, W. Paszkowicz, A. Suchocki, B. G. Svensson, and R. Yakimova, J. Cryst. Growth **308**(1), 93 (2007).
[20] K. Bang, D. Hwang, and J. Myoung, Appl. Surf. Sci. **207**(1–4), 359 (2003).

Published under an exclusive license by AIP Publishing

Downloaded from http://pubs.aip.org/aip/apl/article-pdf/doi/10.1063/5.0147948/17720396/212101_1_5.0147948.pdf

[21] J. Toft and O. M. Kvalheim, Chemom. Intell. Lab. Syst. **19**(1), 65 (1993).
[22] T. Zheng, W. He, L. Wang, J. Li, and S. Zheng, J. Cryst. Growth **533**, 125455 (2020).
[23] W. Mi, C. Luan, Z. Li, C. Zhao, X. Feng, and J. Ma, Opt. Mater. **35**(12), 2624 (2013).
[24] Q. Shi, Q. Wang, D. Zhang, Q. Wang, S. Li, W. Wang, Q. Fan, and J. Zhang, J. Lumin. **206**, 53 (2019).
[25] Y. Wang, P. T. Dickens, J. B. Varley, X. Ni, E. Lotubai, S. Sprawls, F. Liu, V. Lordi, S. Krishnamoorthy, and S. Blair, Sci. Rep. **8**(1), 18075 (2018).
[26] X.-X. Li, G. Zeng, Y.-C. Li, H. Zhang, Z.-G. Ji, Y.-G. Yang, M. Luo, W.-D. Hu, D. W. Zhang, and H.-L. Lu, npj Flexible Electron. **6**(1), 47 (2022).
[27] B. Tak, M. Garg, S. Dewan, C. G. Torres-Castanedo, K.-H. Li, V. Gupta, X. Li, and R. Singh, J. Appl. Phys. **125**(14), 144501 (2019).
[28] A. S. Pratiyush, S. Krishnamoorthy, R. Muralidharan, S. Rajan, and D. N. Nath, *Gallium Oxide: Technology, Devices and Applications*, edited by S. Pearton, F. Ren, and M. Mastro (Elsevier, 2018), p. 369.
[29] C. Fares, F. Ren, and S. J. Pearton, ECS J. Solid State Sci. Technol. **8**(7), Q3007 (2019).
[30] H. Sheoran, B. Tak, N. Manikanthababu, and R. Singh, ECS J. Solid State Sci. Technol. **9**(5), 055004 (2020).
[31] S. M. Sze, Y. Li, and K. K. Ng, *Physics of Semiconductor Devices* (John Wiley & Sons, 2021).

Downloaded from http://pubs.aip.org/aip/apl/article-pdf/doi/10.1063/5.0147948/17720396/212101_1_5.0147948.pdf

Published under an exclusive license by AIP Publishing